frontiers | Frontiers in Energy Research

TYPE Original Research
PUBLISHED 15 November 2023
DOI 10.3389/fenrg.2023.1308750

OPEN ACCESS

EDITED BY
Muhammad Zeeshan Malik,
Taizhou University, China

REVIEWED BY
Liansong Xiong,
Xi'an Jiaotong University, China
Qinglei Bu,
Xi'an Jiaotong-Liverpool University, China

*CORRESPONDENCE
Lu Qu,
qulu@tsinghua.edu.cn

RECEIVED 07 October 2023
ACCEPTED 26 October 2023
PUBLISHED 15 November 2023

CITATION
Chen Y, Qu L, Yu Z, Zhao B, Kang Q, Cui K and Zeng R (2023), Research on the loss characteristics of high-voltage cascaded energy storage systems based on IGCTs. *Front. Energy Res.* 11:1308750. doi: 10.3389/fenrg.2023.1308750

Research on the loss characteristics of high-voltage cascaded energy storage systems based on IGCTs

Yushuo Chen, Lu Qu*, Zhanqing Yu, Biao Zhao, Qian Kang, Kangsheng Cui and Rong Zeng

Department of Electrical Engineering, Tsinghua University, Beijing, China

High-voltage cascaded energy storage systems have become a major technical direction for the development of large-scale energy storage systems due to the advantages of large unit capacity, high overall efficiency, satisfactory economy, reliable safety, and easy access to grid dispatching. The loss characteristics analysis is the design basis of the water-cooling system of a high-voltage cascaded energy storage system, and its accurate calculation can determine the system's safe and reliable operation of the system. This paper first introduces the four-quadrant operation principles of a cascaded H-bridge energy storage system, and analyzes the calculation method of the loss of the Integrated Gate-Commutated Thyristor based power module; On this basis, it studies the loss characteristics of the cascaded energy storage system and analyzes the influence of different modulation strategies and third harmonic injection on the loss characteristics of the energy storage system; Finally, this paper has completed the loss test for the engineering prototype module and compared the test results with theoretical calculation results to verify the accuracy of the loss calculation method of the high-voltage cascaded energy storage system.

KEYWORDS

high-voltage cascade H-bridge, direct-mounted, energy storage system, IGCT, loss characteristics

1 Introduction

As is known to all, large-scale development of new energy sources is an inevitable path to achieve 'emission peak' and 'carbon neutrality' (Liu et al., 2020a; Li et al., 2021). However, it cannot be ignored that due to the characteristics of renewable energy such as intermittency, fluctuation and randomness, it is difficult to provide stable power after being connected to the grid, and problems such as poor grid stability and deteriorated power quality may also occur (He et al., 2022; Li et al., 2022).

With the maturity of new energy power generation and battery manufacturing, energy storage technology has emerged to provide solutions to problems such as deterioration of power quality and poor stability caused by large-scale new energy sources (Maharjan and InoueAkagi, 2008; Liu et al., 2020b). Among these solutions, high-voltage cascaded energy storage systems have recently attracted the attention of academic and industrial circles due to the strengths of large unit capacity, high overall efficiency, satisfactory economy, reliable safety and easy access to grid dispatching. Literature Chatzinikolaou and Rogers (2016) designed a battery balancing strategy for the H-bridge cascade conversion structure to

eliminate the influence of battery internal resistance and transient electrochemical phenomena. Literature Ota et al. (2016) targets a modular cascaded multi-level battery energy storage system with a single star bridge unit component, effectively reducing the use of harmonic filters and AC side transformers. Literature Busarello et al. (2017) proposes a battery energy storage system with 8 H-bridge converter structures. This system can be connected to the distributed distribution network without the need for high-power transformers. Literature Jiang et al. (2018) proposes a hybrid energy storage system and control method, improving the front space vector control technology to achieve direct active power allocation and charge state balance of the capacitor. It can be seen that the current cascaded multi-level chain energy storage system mainly focuses on the optimized design of the cascade structure, energy storage AC and DC control technology, *etc.*, and there is relatively little research on loss characteristics.

With the continuous development of power electronic devices, integrated gate commutated thyristors (IGCTs) have been widely used in large-capacity converter systems and other devices due to their high current-carrying capacity, low on-state loss and high reliability (Filsecker et al., 2013; Zeng et al., 2018). Meanwhile, with the continuous increase in the capacity of energy storage systems, the advantages of IGCTs', such as large capacity and high reliability, make them quite suitable for the development of high-voltage cascaded energy storage converters with large capacity.

The increase in the capacity of energy storage systems has also led to a significant increase in power devices losses, and the system loss and heat dissipation of the systems play a critical role in the safe and reliable operation of energy storage systems (Zhao et al., 2015; Huang, 2017). Currently, there are a considerable number of studies on the loss of insulated gate bipolar thyristors (IGBTs). Literature (Xu et al., 2002; Rajapakse et al., 2005) established a switching loss model based on the relationship between IGBT transient voltage and current, and the calculation is complicated; Literature (Li et al., 2015) studied the calculation method of the loss of different three-level topology, which has a certain guiding significance; Literature (Luo et al., 2018) studied the calculation of the loss of different three-level modulation strategies, which optimizes the loss characteristics of the converters and the system efficiency. Given the fact that research on the loss characteristics of IGCTs is mostly limited to DC circuit breakers, var compensators, three-level converters, and modular multilevel converters (MMCs) (Meyer and Rufer, 2006; Li et al., 2007; Chen et al., 2016), literature (Guo et al., 2021) adopted the equivalent average method to evaluate the loss of MMCs based on IGCT devices; Literature (Wei et al., 2022a) considered the influence of voltage and current harmonic content on the calculation of loss under high voltage and high current, and analyzed the loss characteristics of high power neutral-point clamped three-level converters based on IGCTs; Literature (Wei et al., 2022b) studied the influence of different test operation conditions on the dynamic characteristic parameters of IGCTs, and presented a numerical model of IGCT loss considering device voltage, current, and temperature. However, since there is still less research on the loss characteristics of IGCTs in large capacity high-voltage cascaded energy storage systems, it is essential to calculate and analyze the loss of high-voltage cascaded energy storage systems based on IGCTs.

This paper is a research on the loss characteristics of high-voltage cascaded energy storage systems based on IGCTs, which first introduces the four quadrant operating principles of a energy storage system and analyzes the calculation method of the loss of the IGCT power device; On this basis, it studies the loss characteristics of the energy storage system and analyzes the influence of different modulation strategies and third harmonic injection on the loss characteristics of the energy storage system; Finally, this paper verifies the accuracy of the calculation method by comparing the numerical examples with the actual engineering data, so as to provide a theoretical reference for the subsequent different topologies of energy storage systems, the efficiency optimization of modulation strategies and the cooling system design.

2 The high-voltage cascaded energy storage system's basic principles

The topology diagram of a cascaded energy storage system is shown in Figure 1 which presents a three-phase star arrangement. Each phase is cascaded by N power units, and each power unit consists mainly of an H-bridge circuit, a DC filter interface circuit, and a battery pack. The energy storage battery pack is connected in parallel at both ends of the DC capacitor of the H-bridge circuit through the filter interface circuit. By adjusting the amplitude and phase of the output voltage on the AC side of the bridge circuit, the active and reactive power exchange with the AC system can be realized.

Figure 2 shows the four-quadrant operation diagram of the high-voltage cascaded energy storage system, where U_S is the grid-side voltage, U_I is the valve-side voltage, and I_L is the inductor current. The cascaded energy storage system which relies on its large number of modules rather than high switching frequency to achieve low harmonic voltage output, avoids the shortcoming of low switching frequency of IGCTs and can fully exploit the advantage of low on-state loss of IGCTs.

3 Method of calculating the loss of the IGCT power unit

Unlike conventional voltage-controlled IGBT devices, the analysis and calculation process of the IGCT module's loss is more complicated, this is because the switching process of IGCTs is similar to that of thyristors, whose switching rate cannot be controlled by the gate drive circuit. Therefore, the anode reactor must be connected in series in the conversion loop to limit the rate of current change when the device is switched on, and the RCD clamping circuit should be configured to absorb the inductor's energy.

The circuit of the IGCT full-bridge module is shown in Figure 3, where C_H is the DC-link capacitor and L is the anode inductance. The RCD clamping circuit includes clamping resistance R, clamping capacitance C, and clamping diode D. In the switching circuit part, four IGCT power modules form an H-bridge circuit, T_1-T_4 are IGCTs and D_1-D_4 are reverse parallel diodes, and the losses of the switching circuit mainly include on-state loss and switching loss.

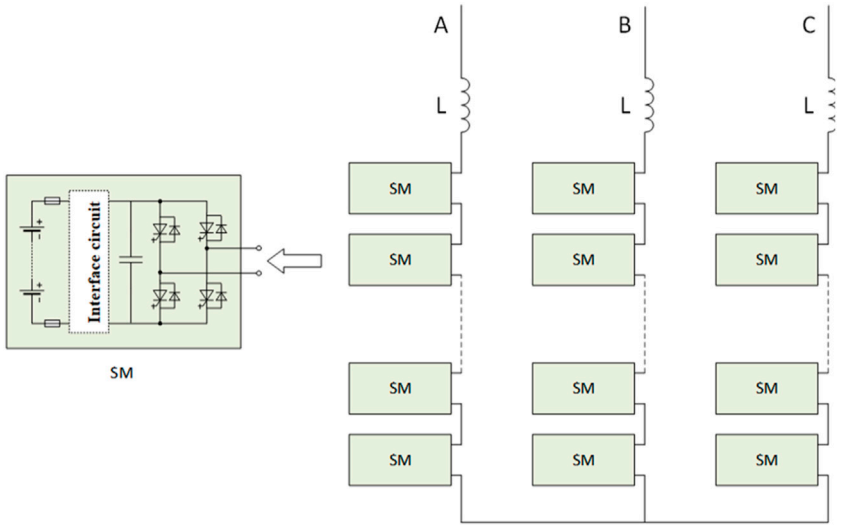

FIGURE 1
Topology diagram of the cascaded energy storage system (star configuration).

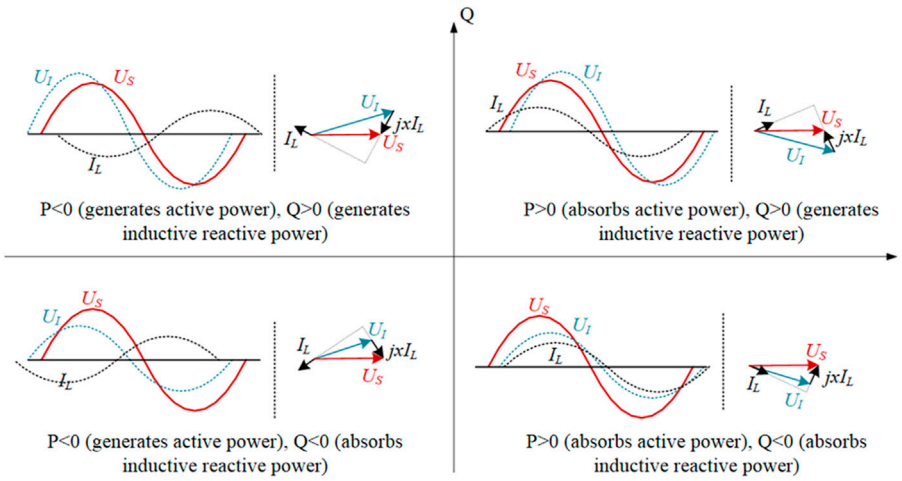

FIGURE 2
Four-quadrant operating diagram of the cascaded energy storage system.

3.1 On-state loss

A single IGCT or a single reverse parallel diode is only responsible for the flow of positive half-wave (or negative half-wave) current, so the on-state loss of a single IGCT or a single reverse parallel diode is:

$$P_{\mathrm{IGCT\_cond}} = \frac{1}{2\pi}\int_0^{\pi} u_{\mathrm{CE}}(t) i_{\mathrm{C}}(t) \tau(t) dt \quad (1)$$

$$P_{\mathrm{Diode\_cond}} = \frac{1}{2\pi}\int_0^{\pi} u_{\mathrm{F}}(t) i_{\mathrm{C}}(t) \tau(t) dt \quad (2)$$

In the equation, $u_{\mathrm{CE}}(t)$ and $u_{\mathrm{F}}(t)$ are the voltage of both ends of the IGCT and reverse parallel diode, respectively, $i_{\mathrm{C}}(t)$ is the current flowing through the IGCT and reverse parallel diode, and $\tau(t)$ is the duty ratio of the IGCT and reverse parallel diode in one period.

$u_{\mathrm{CE}}(t)$ and $i_{\mathrm{C}}(t)$ have a non-linear relationship with $u_{\mathrm{F}}(t)$ and $i_{\mathrm{C}}(t)$, and the typical curve is shown in Figure 4. The relationship between $u_{\mathrm{CE}}(t)$, $i_{\mathrm{C}}(t)$ and $u_{\mathrm{F}}(t)$, $i_{\mathrm{C}}(t)$ is approximated by a straight line as:

$$u_{\mathrm{CE}}(t) = U_{\mathrm{CE0}} + r_{\mathrm{CE}} i_{\mathrm{C}}(t) \quad (3)$$

$$u_{\mathrm{F}}(t) = U_{\mathrm{F0}} + r_{\mathrm{F}} i_{\mathrm{C}}(t) \quad (4)$$

In the equation, U_{CE0} and U_{F} are the conduction threshold voltage of the IGCT and the reverse parallel diode, and r_{CE} and r_{F} are the slope resistance of the IGCT and the reverse parallel diode.

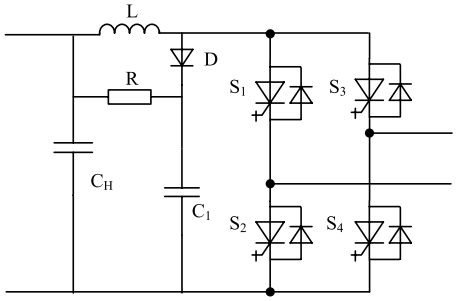

FIGURE 3
The IGCT full-bridge module circuit.

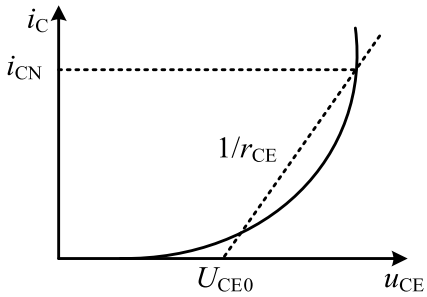

FIGURE 4
Typical curve diagram of u_{CE} and i_C.

3.2 Switching loss

Setting the switching frequency of a single IGCT or a single reverse parallel diode to f_{sw}, then a single IGCT or a single reverse parallel diode should be switched on and off f_{sw} times within half a period. Thus, the switching loss of a single IGCT and a single reverse parallel diode is:

$$P_{\mathrm{IGCT\_sw}} = \frac{1}{\pi}\sum_{n=1}^{f_{sw}}\left(E_{\mathrm{IGCT\_sw(on)}} + E_{\mathrm{IGCT\_sw(off)}}\right) \tag{5}$$

$$P_{\mathrm{Diode\_sw}} = \frac{1}{\pi}\sum_{n=1}^{f_{sw}}\left(E_{\mathrm{Diode\_sw(on)}} + E_{\mathrm{Diode\_sw(off)}}\right) \tag{6}$$

In the equation, $E_{\mathrm{IGCT\_sw(on)}}$ and $E_{\mathrm{IGCT\_sw(off)}}$ are the IGCT's lost energy when switched on and off once, respectively, and $E_{\mathrm{Diode\_sw(on)}}$ (on) and $E_{\mathrm{Diode\_sw(off)}}$ are that of the reverse parallel diode.

In General, the energy lost when the IGCT or reverse parallel diode is switched on or off varies non-linearly with the current, which makes it difficult to describe the energy lost accurately and quantitatively with analytical expressions. To simplify the calculation, the energy lost by the IGCT or reverse parallel diode when switched each time is generally expressed as a function of the current and DC voltage flowing through the device, that is:

$$\begin{aligned} E_{\mathrm{sw}} &= E_{\mathrm{sw(on)}} + E_{\mathrm{sw(off)}} \\ &= E_{\mathrm{sw}}(I, U_{\mathrm{DC}}) = \left(a + bI + cI^2\right)\frac{U_{\mathrm{DC}}}{U_{\mathrm{Test}}} \end{aligned} \tag{7}$$

In the equation, a, b, and c are the polynomial coefficients of the energy and current consumed by each switching, which can be obtained directly from the device data sheet or fitted by the loss curve; U_{DC} is the DC voltage endured by the device in actual operation; U_{Test} is the DC voltage during the loss curve test.

Hence, the switching loss of the IGCT and reverse parallel diode can be expressed as:

$$P_{\mathrm{IGCT\_sw}} = f_{\mathrm{sw}}\left(\frac{a_{\mathrm{IGCT}}}{2} + \frac{b_{\mathrm{IGCT}}}{\pi}\sqrt{2}\,I + \frac{c_{\mathrm{IGCT}}}{2}I^2\right)\frac{U_{\mathrm{DC}}}{U_{\mathrm{IGCT\_Test}}} \tag{8}$$

$$P_{\mathrm{Diode\_sw}} = f_{\mathrm{sw}}\left(\frac{a_{\mathrm{Diode}}}{2} + \frac{b_{\mathrm{Diode}}}{\pi}\sqrt{2}\,I + \frac{c_{\mathrm{Diode}}}{2}I^2\right)\frac{U_{\mathrm{DC}}}{U_{\mathrm{Diode\_Test}}} \tag{9}$$

4 Method of calculating the loss of the cascaded energy storage system

4.1 H-bridge conversion mode

The conversion method of the H-bridge topology is analyzed based on the circuit diagram of the IGCT full-bridge module shown in Figure 3. The switching status, output voltage u_{ab} and output current i_{ab} of the IGCT and reverse parallel diode in the H-bridge topology under different operating conditions are shown in Table 1. In Table 1, operating conditions one to eight correspond to Figure 5 (a)-5 (h).

Figure 6 displays the phase relationship between the modulating wave and the load current when the converter is under inductive load, where φ represents the power factor angle. According to the zero crossing point of voltage and current, a fundamental wave period can be divided into four sections, then by analyzing the current path of each section, the conduction interval of each device can be obtained.

The duty ratio of the IGCT and reverse parallel diode in one period of the H-bridge is then analyzed according to different modulation strategies.

4.2 The conduction law of the H-Bridge's topology with the unipolar modulation method

The schematic diagram of the unipolar modulation method is presented in Figure 7. In the first period, T_1 and T_2 are alternately conducted for half a period, and T_3 and T_4 operate at the carrier frequency; In the second period, T_3 and T_4 are alternately conducted for half a period, and T_1 and T_2 operate at the carrier frequency. The analysis is performed through taking the first period as an example.

When the H-bridge is operating at $[0, \pi\text{-}\varphi]$, the modulation voltage is positive and the load current is positive. At this time, the output state of the H-bridge switches between $u(t) > 0$, $i(t) > 0$ and $u(t) = 0$, $i(t) > 0$. The current flow diagram is shown in Figure 5 (a) and (b). At this moment, there is a switching between T_4 and D_3, and T_1 has been in the on state.

When the H-bridge is operating at $[\pi\text{-}\varphi, \pi]$, the modulation voltage is negative and the load current is positive. At this time, the output state of the H-bridge switches between $u(t) < 0$, $i(t) > 0$ and $u(t) = 0$, $i(t) > 0$. The current flow diagram is shown in Figure 5 (c) and (d). At this moment, there is a switching between T_4 and D_3, and D_2 has been in the on state.

When the H-bridge is operating at $[\pi, 2\pi\text{-}\varphi]$, the modulation voltage is negative and the load current is negative. At this time, the output state of

TABLE 1 The H-bridge topology's switching status.

Operation condition	1	2	3	4	5	6	7	8
Conduction device	T_1, T_4	T_1, D_3	D_2, D_3	T_4, D_2	T_2, T_3	T_2, D_4	D_1, D_4	T_3, D_1
i_{ab}	$i_{ab} > 0$	$i_{ab} > 0$	$i_{ab} > 0$	$i_{ab} > 0$	$i_{ab} < 0$	$i_{ab} < 0$	$i_{ab} < 0$	$i_{ab} < 0$
u_{ab}	$u_{ab} > 0$	$u_{ab} = 0$	$u_{ab} < 0$	$u_{ab} = 0$	$u_{ab} < 0$	$u_{ab} = 0$	$u_{ab} > 0$	$u_{ab} = 0$

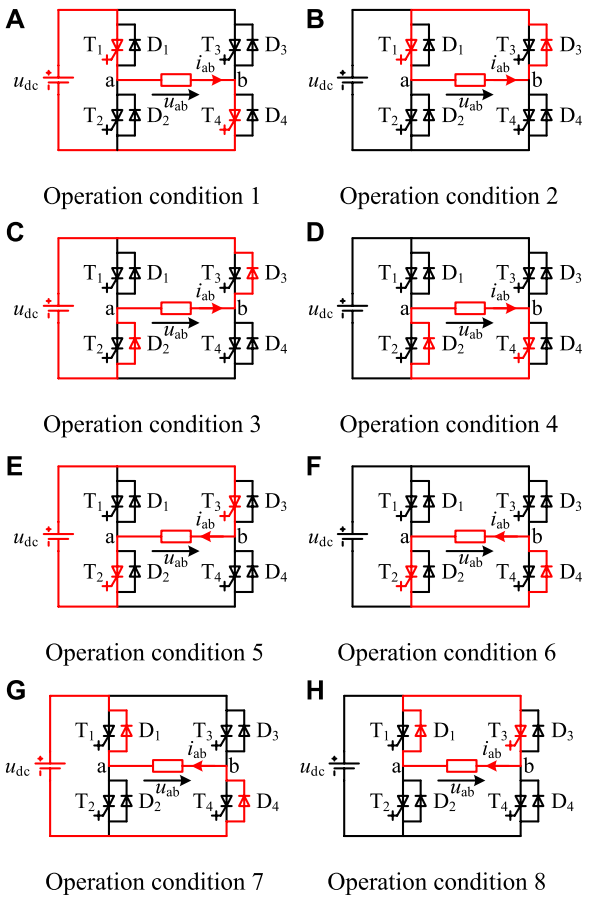

FIGURE 5
The H-bridge topology's conversion method. **(A)** Operation condition 1 **(B)** Operation condition 2 **(C)** Operation condition 3 **(D)** Operation condition 4 **(E)** Operation condition 5 **(F)** Operation condition 6 **(G)** Operation condition 7 **(H)** Operation condition 8.

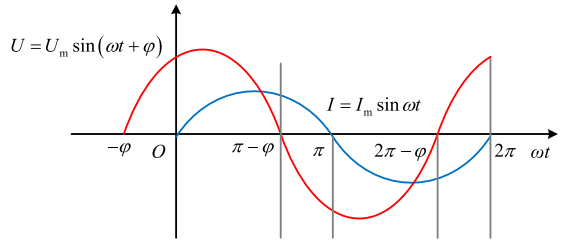

FIGURE 6
Phase relationship between the modulating wave and load current.

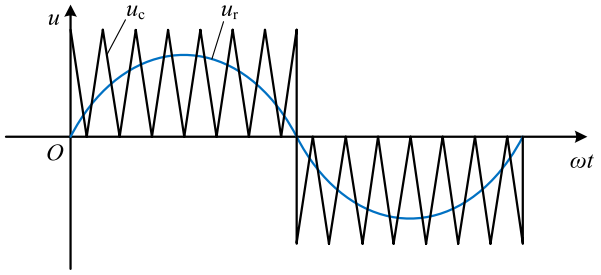

FIGURE 7
The schematic diagram of the unipolar modulation method.

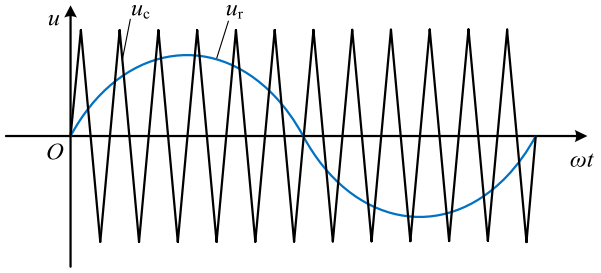

FIGURE 8
The schematic diagram of the bipolar modulation method.

the H-bridge switches between $u(t) < 0$, $i(t) < 0$ and $u(t) = 0$, $i(t) < 0$. The current flow diagram is shown in Figure 5 (e) and (f). At this moment, there is a switching between T_3 and D_4, and T_2 has been in the on state.

When the H-bridge is operating at $[2\pi\text{-}\varphi, 2\pi]$, the modulation voltage is positive and the load current is negative. At this time, the output state of the H-bridge switches between $u(t) > 0$, $i(t) < 0$ and $u(t) = 0$, $i(t) < 0$. The current flow diagram is shown in Figure 5 (g) and (h). At this moment, there is a switching between T_3 and D_4, and D_1 has been in the on state.

4.3 The conduction law of the H-Bridge's topology with the bipolar modulation method

A schematic diagram of the bipolar modulation method is shown in Figure 8. When the H-bridge is operating at $[0, \pi]$, the load current is positive and the modulation voltage is positive at $[0, \pi\text{-}\varphi]$ and negative at $[\pi\text{-}\varphi, \pi]$. The output state of the H-bridge switches between $u(t) > 0$, $i(t) > 0$ and $u(t) < 0$, $i(t) > 0$. The current

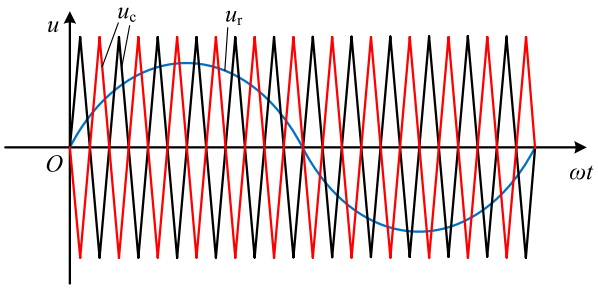

FIGURE 9
The schematic diagram of the unipolar frequency multiplication modulation method.

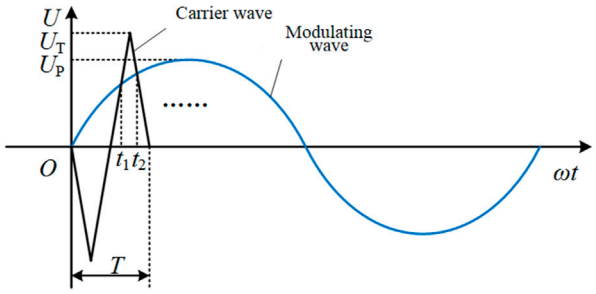

FIGURE 10
The schematic diagram of a carrier period with the bipolar modulation method.

flow diagram is shown in Figure 5 (a) and (c). At this moment, T_1, T_4 and D_2, D_3 are alternately conducted; When the H-bridge is operating at [π, 2π], the load current is negative and the modulation voltage is negative at [π, 2π-φ] and negative at [2π-φ, 2π]. The output state of the H-bridge switches between $u(t) > 0$, $i(t) < 0$, and $u(t) < 0$, $i(t) < 0$. The current flow diagram is shown in Figure 6 (e) and (g). At this moment, T_2, T_3 and D_1, D_4 are alternately conducted.

4.4 The conduction law of the H-Bridge's topology with the unipolar frequency multiplication modulation method

A schematic diagram of the unipolar frequency multiplication modulation method is shown in Figure 9. When the H-bridge is operating at [0, π-φ], the modulation voltage is positive and the load current is positive. At this time, the output state of the H-bridge switches between $u(t) > 0$,$i(t) > 0$ and $u(t) = 0$, $i(t) > 0$. The current flow diagram is shown in Figure 8 (a), (b), and (d). At this moment, T_1 and D_3, T_1 and T_4, T_4 and D_2 are alternately conducted.

When the H-bridge is operating at [π-φ, π], the modulation voltage is negative and the load current is positive. At this time, the output state of the H-bridge switches between $u(t) < 0$, $i(t) > 0$ and $u(t) = 0$, $i(t) > 0$. The current flow diagram is shown in Figure 5 (b), (c), and (d). At this moment, T_1 and D_3, D_2 and D_3, T_4 and D_2 are alternately conducted.

When the H-bridge is operating at [π, 2π-φ], the modulation voltage is negative and the load current is negative. At this time, the output state of the H-bridge switches between $u(t) < 0$, $i(t) < 0$ and $u(t) = 0$, $i(t) < 0$. The current flow diagram is shown in Figure 5 (e), (f), and (h). At this moment, T_3 and D_1, T_2 and T_3, T_2 and D_4 are alternately conducted.

When the H-bridge is operating at [2π-φ, 2π], the modulation voltage is positive and the load current is negative. At this time, the output state of the H-bridge switches between $u(t) > 0$, $i(t) < 0$ and $u(t) = 0$, $i(t) < 0$. The current flow diagram is shown in Figure 5 (f), (g), and (h). At this moment, T_3 and D_1, D_1 and D_4, T_2 and D_4 are alternately conducted.

4.5 Calculation of on-state loss of the H-Bridge power unit

After analyzing the conduction law of the H-bridge's topology with different modulation methods, the duty ratio of different devices can be calculated separately using different modulation strategies. The calculation is performed with T_1using the bipolar modulation method as an example.

Figure 10 is the schematic diagram of the bipolar modulation method, and only one carrier period is drawn in the figure. The equations of carrier line 1 and 2 can be obtained from Figure 10:

$$\begin{cases} u = -2U_T + \dfrac{4U_T}{T}t \\ u = 4U_T - \dfrac{4U_T}{T}t \end{cases} \tag{10}$$

In the equation, T is the carrier period, and U_T is the carrier amplitude.

At t_1 and t_2, it satisfies the equations shown in equation (11):

$$\begin{cases} U_m \sin(\omega t + \varphi) = -2U_T + \dfrac{4U_T}{T}t \\ U_m \sin(\omega t + \varphi) = 4U_T - \dfrac{4U_T}{T}t \end{cases} \tag{11}$$

The duty ratio can be derived from equation (11), see equation (12):

$$\tau(t) = 1 - \frac{t_2 - t_1}{T} = \frac{1 + m\sin(\omega t + \varphi)}{2} \tag{12}$$

Using the above calculation method, the duty ratio corresponding to the conduction angle of each switching device in the H-bridge circuit can be obtained when applying different modulation strategies. It can be noticed that the duty ratios of the conduction angle corresponding to the bipolar modulation method and the unipolar frequency multiplication modulation method in one period are the same. After averaging with the unipolar modulation method in two periods, the duty ratio of the corresponding conduction angle is the same as that of the bipolar modulation method and unipolar frequency multiplication modulation method. Accordingly, although the conduction states are different when the H-bridge circuit adopts different modulation strategies, the duty ratios corresponding to the conduction angle of each switching device remain the same, as can be seen in Table 2.

When the power device is in the on-state and there is current flowing through, loss will be generated. In this way, by using the above-mentioned calculation method of the power device's loss and the calculation of the duty ratio under different modulation

TABLE 2 The duty ratio of the conduction angle corresponding to each device in the H-bridge power unit.

Device	[0, π-φ]	[π-φ, π]	[π, 2π-φ]	[2π-φ, 2π]
T_1	$\frac{1+m\sin(\omega t+\varphi)}{2}$	$\frac{1+m\sin(\omega t+\varphi)}{2}$	—	—
T_2	—	—	$\frac{1-m\sin(\omega t+\varphi)}{2}$	$\frac{1-m\sin(\omega t+\varphi)}{2}$
T_3	—	—	$\frac{1-m\sin(\omega t+\varphi)}{2}$	$\frac{1-m\sin(\omega t+\varphi)}{2}$
T_4	$\frac{1+m\sin(\omega t+\varphi)}{2}$	$\frac{1+m\sin(\omega t+\varphi)}{2}$	—	—
D_1	—	—	$\frac{1+m\sin(\omega t+\varphi)}{2}$	$\frac{1+m\sin(\omega t+\varphi)}{2}$
D_2	$\frac{1-m\sin(\omega t+\varphi)}{2}$	$\frac{1-m\sin(\omega t+\varphi)}{2}$	—	—
D_3	$\frac{1-m\sin(\omega t+\varphi)}{2}$	$\frac{1-m\sin(\omega t+\varphi)}{2}$	—	—
D_4	—	—	$\frac{1+m\sin(\omega t+\varphi)}{2}$	$\frac{1+m\sin(\omega t+\varphi)}{2}$

methods, the average on-state loss of the switch transistor in one period can be calculated.

By substituting the duty ratio and equations (3) and (4) in Table 1 into equations (1) and (2), after integration, the on-state loss of the IGCT and reverse parallel diode of the H-bridge power device can be obtained and shown as follows:

$$P_{\mathrm{IGCT\_cond}} = \left(\frac{1}{2\pi} + \frac{m\cos\varphi}{8}\right)U_{\mathrm{CE0}}I_{\mathrm{CP}} + \left(\frac{1}{8} + \frac{m\cos\varphi}{3\pi}\right)r_{\mathrm{CE}}I_{\mathrm{CP}}^2 \quad (13)$$

$$P_{\mathrm{Diode\_cond}} = \left(\frac{1}{2\pi} - \frac{m\cos\varphi}{8}\right)U_{\mathrm{F0}}I_{\mathrm{CP}} + \left(\frac{1}{8} - \frac{m\cos\varphi}{3\pi}\right)r_{\mathrm{F}}I_{\mathrm{CP}}^2 \quad (14)$$

Therefore, the H-bridge power unit's on-state loss is:

$$P_{\mathrm{cond}} = 4\left(P_{\mathrm{IGCT\_cond}} + P_{\mathrm{Diode\_cond}}\right) \quad (15)$$

4.6 Calculation of switching loss of the H-Bridge power unit

According to the analysis of the H-bridge's conversion mode, it can be found that when the H-bridge modulation strategy is unipolar modulation, T_1, T_2, D_1, and D_2 are switched on and off once, and other switch transistors are switched on and off with a switching frequency of f_{sw}; While when the H-bridge operates with the bipolar modulation method and unipolar frequency multiplication modulation method, all switch transistors of the H-bridge are switched on and off with a switching frequency of f_{sw}. Thus, with the unipolar modulation method, the H-bridge's switching loss is lower. However, under the same carrier frequency, there is higher equivalent output frequency of the unipolar frequency multiplication modulation method and better harmonic performance, so this modulation method is commonly used in engineering. The switching loss of the H-bridge power unit under bipolar modulation and unipolar frequency multiplication modulation is obtained by refering to the calculation method for the switching loss of the IGCT and reverse parallel diode in Section 2:

$$P_{\mathrm{sw}} = 4\left(P_{\mathrm{IGCT\_sw}} + P_{\mathrm{Diode\_sw}}\right) \quad (16)$$

The H-bridge power unit's total loss can be expressed as:

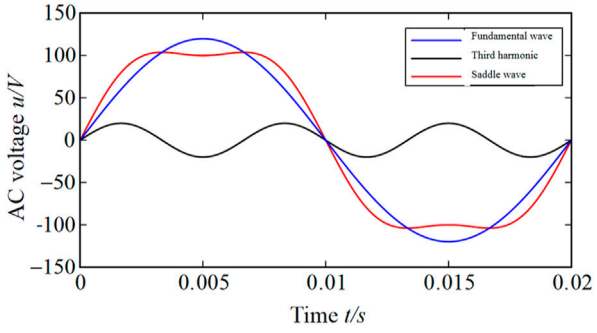

FIGURE 11
Modulating waveform before and after the third harmonic injection.

$$\begin{aligned} P_{\mathrm{PE}} &= P_{\mathrm{cond}} + P_{\mathrm{sw}} \\ &= 4\left(P_{\mathrm{IGCT\_cond}} + P_{\mathrm{Diode\_cond}} + P_{\mathrm{IGCT\_sw}} + P_{\mathrm{Diode\_sw}}\right) \end{aligned} \quad (17)$$

4.7 Influence of third harmonic injection modulation on the H-Bridge power unit loss

Considering that the use of sinusoidal signal for the modulating wave will cause the DC voltage utilization rate to decrease, in actual engineering, when the common star arrangement is used on the load side, the third harmonic injection method is usually adopted to improve the defects of low DC voltage utilization (Zhao et al., 2019; Bieber et al., 2023).

The third harmonic injection strategy is to superimpose a sinusoidal wave of three times the frequency on the modulation fundamental wave, and the synthesized modulating waveform is a saddle wave, as shown in Figure 11. After applying third harmonic injection into the sinusoidal modulation signal, the modulation voltage function can be expressed as:

$$\begin{aligned} u_{\mathrm{p3}}(t) &= u_{\mathrm{r}}(t) + u_{\mathrm{i3}}(t) \\ &= mU_{\mathrm{m}}\left(\sin(\omega t + \varphi) + k\sin\left(3(\omega t + \varphi)\right)\right) \end{aligned} \quad (18)$$

In the equation, k is the injection amount of the third harmonic, and it is the ratio of the amplitude of the injected third harmonic to the amplitude of the fundamental wave.

According to the superposition theorem, the saddle wave can be devided into the fundamental sinusoidal modulating signal and the third harmonic modulating signal, and then the calculation of loss is performed separately. In this way, the calculation equation of loss after injecting the third harmonic can be obtained. Since the calculation method is the same as the above method, the calculation expression is presented directly in this section without further elaboration. After the third harmonic injection, the on-state loss of the IGCT and the reverse parallel diode of the H-bridge power unit can be expressed as follows:

$$\begin{aligned} P_{\mathrm{IGCT\_cond\_3}} = &\left(\frac{1}{2\pi} + \frac{m\cos\varphi}{8}\right)U_{\mathrm{CE0}}I_{\mathrm{CP}} \\ &+\left(\frac{1}{8} + \frac{m\cos\varphi\left(5 - 4k\cos^2\varphi + 3k\right)}{15\pi}\right)r_{\mathrm{CE}}I_{\mathrm{CP}}^2 \end{aligned} \quad (19)$$

TABLE 3 Device characteristic parameters and system parameters.

Parameters	Value
U_{DC}/V	1,152
I/A	2,333
f_{sw}/Hz	300
m	0.95
k	0
U_{CE0}/V	1.22
r_{CE}/mΩ	0.28
U_{F0}/V	1
r_F/mΩ	0.4
a_{IGCT}	1.8
b_{IGCT}	1/150
c_{IGCT}	0
a_{Diode}	14
b_{Diode}	1/1,000
c_{Diode}	0
U_{IGCT_Test}/V	2,800
U_{Diode_Test}/V	2,800

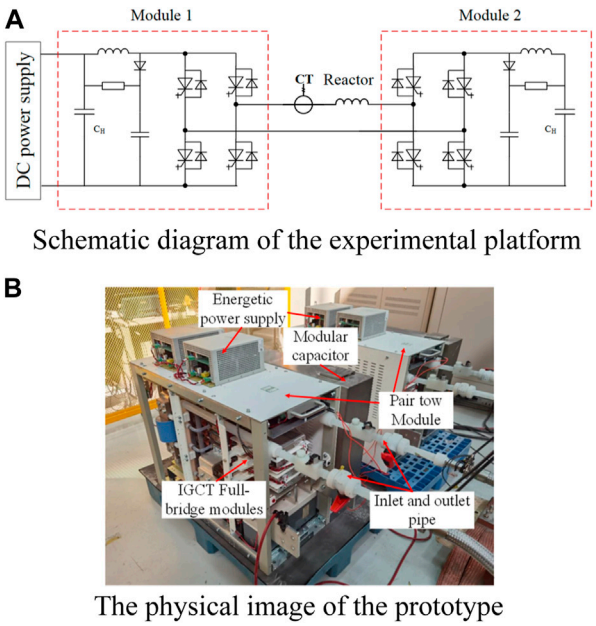

FIGURE 12
The schematic of the experimental platform and the physical image of the prototype. **(A)** Schematic diagram of the experimental platform **(B)** The physical image of the prototype.

$$P_{Diode\_cond\_3} = \left(\frac{1}{2\pi} - \frac{m\cos\varphi}{8}\right)U_{F0}I_{CP} + \left(\frac{1}{8} - \frac{m\cos\varphi\left(5 - 4k\cos^2\varphi + 3k\right)}{15\pi}\right)r_F I_{CP}^2 \quad (20)$$

The switching losses of the IGCT and reverse parallel diode remain unchanged, see equations (8) and (9). Therefore, the total loss of the H-bridge unit after the third harmonic injection is:

$$P_{PE\_3} = P_{cond\_3} + P_{sw} = 4\left(P_{IGCT\_cond\_3} + P_{Diode\_cond\_3} + P_{IGCT\_sw} + P_{Diode\_sw}\right) \quad (21)$$

From the above analysis, it can be learned that the loss of the power semiconductor unit is not only related to factors such as IGCT parameters, reverse parallel diode parameters, and modulation ratio m, but also related to the third harmonic injection amount k.

5 Numerical example analysis and experiment verification

5.1 Numerical example analysis

From the analysis in Sections 2 and 3, it can be seen that in addition to the characteristic parameters of the IGCT and the reverse parallel diode, the factors that affect the loss of the H-bridge include the modulation ratio m, the third harmonic injection amount k, the power factor φ, the current amplitude I_m, and the DC voltage U_{DC}. In order to accurately evaluate the loss characteristics of the power module of the cascaded energy storage system and optimize the design, the loss calculation method needs to be evaluated and verified.

This paper takes the H-bridge that is studied as the analysis object, *t* Power-SC7. $CA_C5000\text{-}45$ Plus is taken as the IGCT module and FY_B 2000-45-02 as the reverse parallel diode module based on actual engineering project needs. The input variables of loss calculation in accordance with the device data sheet (the device parameters are extracted with reference to a junction temperature of 125°C) and engineering system parameters are shown in Table 3.

Through the parameters in Table 3 and equations (8) and (9), (13) and (14), the on-state loss and switching loss of the IGCT and reverse parallel diode can be calculated separately:

$$P_{IGCT\_cond} = \left(\frac{1}{2\pi} + \frac{m\cos\varphi}{8}\right)U_{CE0}I_{CP} + \left(\frac{1}{8} + \frac{m\cos\varphi}{3\pi}\right)r_{CE}I_{CP}^2 = 1021.6\text{W} \quad (22)$$

$$P_{Diode\_cond} = \left(\frac{1}{2\pi} - \frac{m\cos\varphi}{8}\right)U_{F0}I_{CP} + \left(\frac{1}{8} - \frac{m\cos\varphi}{3\pi}\right)r_F I_{CP}^2 = 1069.4\text{W} \quad (23)$$

$$P_{IGCT\_sw} = f_{sw}\left(\frac{a_{IGCT}}{2} + \frac{b_{IGCT}}{\pi}\sqrt{2}\,I + \frac{c_{IGCT}}{2}I^2\right)\frac{U_{DC}}{U_{IGCT\_Test}} = 975.3\text{W} \quad (24)$$

$$P_{Diode\_sw} = f_{sw}\left(\frac{a_{Diode}}{2} + \frac{b_{Diode}}{\pi}\sqrt{2}\,I + \frac{c_{Diode}}{2}I^2\right)\frac{U_{DC}}{U_{Diode\_Test}} = 993.6\text{W} \quad (25)$$

Therefore, the H-bridge power unit's total loss is:

$$P_{PE} = P_{cond} + P_{sw} = 4\left(P_{IGCT\_cond} + P_{Diode\_cond} + P_{IGCT\_sw} + P_{Diode\_sw}\right) = 16.24\text{kW} \quad (26)$$

TABLE 4 Loss test results.

U_{DC}/V	I_{RMS}/A	t_d/min	FIT/(L/min)	T_{in}/°C	T_{out}/°C	ΔT/°C	P/kW	$\bar{P}$/kW
1,155	2,340	—	30.03	14.69	23.34	8.65	18.18	18.11
1,155	2,340	10	30.03	14.50	23.02	8.52	17.91	
1,155	2,340	20	30.03	14.77	23.37	8.60	18.08	
1,155	2,340	30	30.03	15.25	23.94	8.69	18.27	

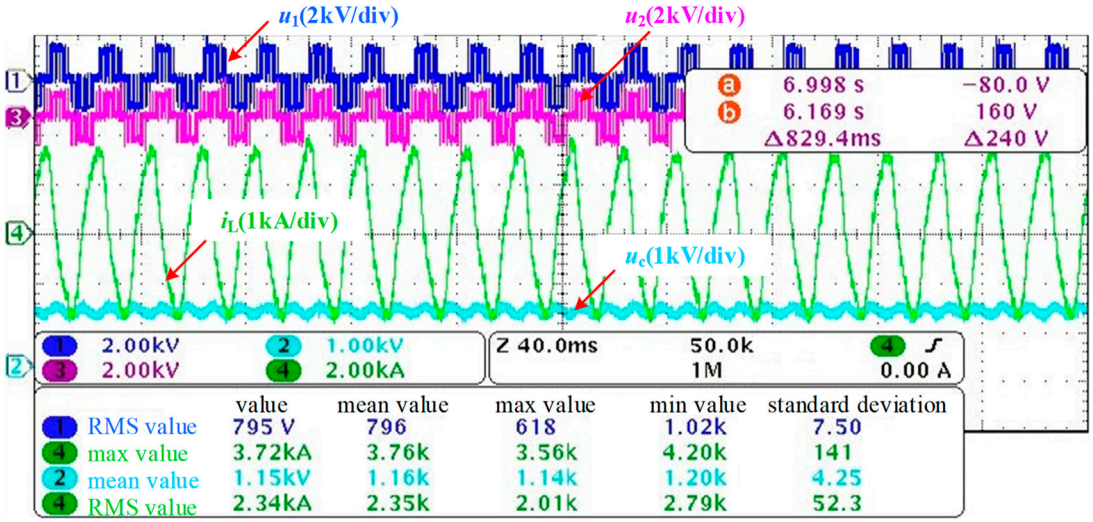

FIGURE 13
Measured waveform diagram.

5.2 Experiment verification

The basic circuit diagram of the experimental platform, shown in Figure 12A, is set up to verify the effectiveness of the loss calculation method in this paper. Module 1 is connected to a DC power supply, and module 2 is the tested module. Module 1 and module 2 are connected by a reactor, and the voltage on the DC side and the current on the AC side of module 2 are adjusted by the control chassis to achieve full load operation between the modules. Module 1 and Module 2 are water cooled. The test modules will generate losses when running, and the measured temperature of the water-cooling system changes with the changes in losses. The loss of the IGCT module can be measured indirectly by measuring the temperature changes in the water-cooling system. The physical image of the prototype is shown in Figure 12 (b), and the loss of the sample module is calculated using the experimental calorimetry method. The experimental results are shown in Table 4.

The measured waveform is shown in Figure 13. In the figure, u_1 and u_2 represent the output voltages of module 1 and module 2, i_L represents the inductor current, and u_c represents the voltage at both ends of the DC-link capacitor C_H.

The measured loss is determined by the following equation:

$$P = C_p{}^{*}FIT{}^{*}\rho{}^{*}\Delta T \tag{27}$$

In the equation, P, kW, is the loss of a single power module; C_p, 4.2 kJ/(kg·°C), is the specific heat capacity of water; FIT, m^3/s, is the flow rate of water; ρ, 1,000 kg/m^3, is the density of water; ΔT is the temperature difference, and $\Delta T = T_{in} - T_{out}$.

In the calculation example, the loss of a single H-bridge power module is 16.24 kW. However, in the actual loss test, the test module must also take into account the effects of the anode inductance, the RCD clamp circuit and the discharge resistor in the water cooling system. Using the actual engineering parameters, the discrete loss Ps of the anode inductor, RCD clamp circuit and discharge resistor can be determined to be 2.1 kW. Therefore, the loss of an IGCT full-bridge module is 18.34kW, which is consistent with the measured average loss of 18.11 kW shown in Table 4.

6 Conclusion

In this paper, by conducting research on the loss characteristics of high-voltage cascaded energy storage systems based on IGCTs, the following conclusions have been drawn:

(1) By studying the duty ratio after adopting different modulation strategies, the calculation equation for the on-state loss of the IGCT power module under different modulation strategies is obtained. The results show that the on-state loss of the IGCT power module is not highly correlated to the modulation strategy, but is related to factors such as IGCT parameters, reverse parallel diode parameters, and modulation ratio m; The switching loss of the IGCT can be

fitted by the equation of the characteristic parameters of the device, and the switching loss is smaller in the unipolar modulation mode. Yet, at the same carrier frequency, the equivalent output frequency of the unipolar frequency multiplication modulation method is higher and the harmonic performance is better. Therefore, the unipolar frequency multiplication modulation method is generally adopted in engineering.

(2) The third harmonic injection method can effectively improve the utilization rate of the voltage on the DC side. Meanwhile, the third harmonic injection amount k will also affect the on-state loss of the power device without affecting the switching loss.

(3) Based on numerical example analysis and engineering measured data, it can be known that the power loss in the theoretical calculation is 18.34 kW, and the measured average loss is 18.11 kW, presenting basically consistent results, which can provide a certain reference value for the subsequent design of the full-bridge module of the high-voltage cascaded energy storage system.

Data availability statement

The original contributions presented in the study are included in the article/Supplementary Material, further inquiries can be directed to the corresponding author.

Author contributions

YC: Investigation, Writing–original draft. LQ: Conceptualization, Writing–review and editing. ZY: Funding acquisition, Writing–review and editing. BZ: Supervision, Writing–review and editing. QK: Validation, Writing–original draft. KC: Data curation, Validation, Writing–review and editing. RZ: Supervision, Writing–review and editing.

Funding

The author(s) declare financial support was received for the research, authorship, and/or publication of this article. The authors declare that financial support was received for the research, authorship, and/or publication of this article. This work was supported by the Inner Mongolia Autonomous Region "Listed and Commanded" Project (grant no. 2023JBGS0013).

Conflict of interest

The authors declare that the research was conducted in the absence of any commercial or financial relationships that could be construed as a potential conflict of interest.

Publisher's note

References

Bieber, L. M., Pfannschmidt, J. A., Wang, L., Jatskevich, J., and Li, W. (2023). A hybrid five-level modular multilevel converter with high efficiency and small energy storage requirements for HVDC transmission. *IEEE Trans. Industrial Electron.* 70 (2), 1597–1608. doi:10.1109/tie.2022.3158006

Busarello, T. D. C., Mortezaei, A., Bubshait, A. S., and Simoes, M. G. (2017). Three-phase battery storage system with transformerless cascaded multilevel inverter for distribution grid applications. *IET Renew. Power Gener.* 11 (6), 742–749. doi:10.1049/iet-rpg.2016.0629

Chatzinikolaou, E., and Rogers, D. J. (2016). Cell SoC balancing using a cascaded full-bridge multilevel converter in battery energy storage systems. *IEEE Trans. Industrial Electron.* 63 (9), 5394–5402. doi:10.1109/tie.2016.2565463

Chen, Z. Y., Yu, Z. Q., Lv, G., Huang, Y. L., Zeng, R., Chen, M., et al. (2016). Research on 10 kV DC hybrid circuit breakers based on IGCT series connection. *Proc. CSEE* 36 (2), 317–326.

Filsecker, F., Alvarez, R., and Bernet, S. (2013). Comparison of 4.5-kV press-pack IGBTs and IGCTs for medium-voltage converters. *IEEE Trans. Industrial Electron.* 60 (2), 440–449. doi:10.1109/tie.2012.2187417

Guo, M. Z., Bai, R. H., Tang, B. J., Zhao, B., Zhou, X. D., Yu, Z. Q., et al. (2021). Analysis and calculation of loss characteristics of IGCT-MMC based on equivalent average. *South. Power Syst. Technol.* 15 (03), 8–14.

He, P., Li, Z., Li, C. S., Fang, Q. Y., and Zheng, M. M. (2022). Modeling of energy storage electromechanical transient characteristics based on virtual synchronous machine technology. *Power Syst. Prot. Control* 50 (07), 11–22.

Huang, A. Q. (2017). Power semiconductor devices for smart grid and renewable energy systems. *Proc. IEEE* 105 (11), 2019–2047. doi:10.1109/jproc.2017.2687701

Jiang, W., Xue, S., Zhang, L., Xu, W., Yu, K., Chen, W., et al. (2018). Flexible power distribution control in an asymmetrical-cascaded-multilevel-converter-based hybrid energy storage system. *IEEE Trans. Industrial Electron.* 65 (8), 6150–6159. doi:10.1109/tie.2017.2787557

Li, G. D., Mao, C. X., Lu, J. M., and Cui, Y. Y. (2007). Research on the DC link of three-level high-voltage inverters based on IGCT series connection. *Proc. CSEE* 27 (1), 82–87.

Li, J. H., Zhang, J. H., Li, C. P., Chen, G. H., and Zhang, H. T. (2021). The configuration plan and economic analysis of the energy storage system involved in peak regulation. *Electr. Eng. Mag.* 36 (19), 4148–4160. doi:10.19595/j.cnki.1000-6753.tces.200678

Li, J. Q., Wang, D., Fan, H., Yang, D. J., Fang, R. C., and Sang, Z. X. (2022). The hierarchical optimization and control method of active distribution network with mobile energy storage. *Automation Electr. Power Syst.* 46 (10), 189–198.

Li, X. S., Zhang, X. W., Chang, Y. F., and Cheng, Z. P. (2015). Research on the reliability of small wind power converters based on semiconductor power loss. *Power Syst. Prot. Control* 43 (19), 15–21.

Liu, C., Sun, T., Cai, G. W., Ge, C. W., Ge, Y. F., Yan, Y. H., et al. (2020). Analysis of the active support control and primary frequency modulation contribution of battery energy storage power stations based on the third-stage model of synchronous machines. *Proc. CSEE* 40 (15), 4854–4866.

Liu, C., Zhuo, J. K., Zhao, D. M., Li, S. Q., Chen, J. S., Wang, J. X., et al. (2020). Research review of the application of energy storage systems to achieve the flexible and safe operation of renewable energy microgrids. *Proc. CSEE* 40 (1), 1–18.

Luo, R., He, Y. J., Chen, H., and Liu, J. J. (2018). SVPWM strategy for neutral-point balancing and low switching loss of three-level converters. *Electr. Eng. Mag.* 33 (14), 3245–3254.

Maharjan, L., Inoue, S., and Akagi, H. (2008). A transformerless energy storage system based on a cascade multilevel PWM converter with star configuration. *IEEE Trans. Industry Appl.* 44 (5), 1621–1630. doi:10.1109/tia.2008.2002180

Meyer, J. M., and Rufer, A. (2006). A DC hybrid circuit breaker with ultra-fast contact opening and integrated gate-commutated thyristors (IGCTs). *IEEE Trans. Power Deliv.* 21 (2), 646–651. doi:10.1109/tpwrd.2006.870981

Ota, J. I. Y., Sato, T., and Akagi, H. (2016). Enhancement of performance, availability, and flexibility of a battery energy storage system based on a modular multilevel cascaded converter (MMCC-SSBC). *IEEE Trans. Power Electron.* 31 (4), 2791–2799. doi:10.1109/tpel.2015.2450757

Rajapakse, A. D., Gole, A. M., and Wilson, P. L. (2005). Electromagnetic transients simulation models for accurate representation of switching losses and thermal performance in power electronic systems. *IEEE Trans. Power Deliv.* 20 (1), 319–327.

Wei, W., Ge, Q. X., Li, Y. H., Zhao, L., and Zhang, B. (2022). Analysis of loss characteristics of high-power three-level neutral-point clamped converters. *Micromotors* 55 (07), 37–44.

Wei, W., Ge, Q. X., Li, Y. H., Zhao, L., and Zhang, B. (2022). Loss model of IGCT devices of high-power traction converters. *Electr. Drive* 52 (19), 11–18.

Xu, D., Lu, H., Huang, L., Azuma, S., Kimata, M., and Uchida, R. (2002). Power loss and junction temperature analysis of power semiconductor devices. *IEEE Trans. Industry Appl.* 38 (5), 1426–1431. doi:10.1109/tia.2002.802995

Zeng, R., Zhao, B., Yu, Z. Q., Song, Q., Huang, Y. L., Chen, Z. Y., et al. (2018). Application prospects for IGCTs in DC grids. *Proc. CSEE* 38 (15), 4307–4317.

Zhao, C., Hu, Y., Luan, K., Xu, F., Li, Z., Wang, P., et al. (2019). Energy storage requirements optimization of full-bridge MMC with third-order harmonic voltage injection. *IEEE Trans. Power Electron.* 34 (12), 11661–11678. doi:10.1109/tpel.2019.2906349

Zhao, C., Yin, H., Yang, Z. P., and Ma, C. B. (2015). Equivalent series resistance-based energy loss analysis of a battery semiactive hybrid energy storage system. *IEEE Trans. Energy Convers.* 30 (3), 1081–1091. doi:10.1109/tec.2015.2418818